Author: Biesiekierski, Arne; Ping, D.H.; Yamabe-Mitarai, Y.; Wen, Cuie
Title: Impact of ruthenium on microstructure and corrosion behavior of b-type Ti-Nb-Ru alloys for biomedical applications
Year: 2014
Journal: Materials and Design
Volume: 59
Pages: 303-309
URL: http://doi.org/10.1016/j.matdes.2014.02.058

Impact of ruthenium on microstructure and corrosion behavior of β -type Ti-Nb-Ru alloys for biomedical applications

Arne Biesiekierski,[1] D.H. Ping,[2] Y. Yamabe-Mitarai[2] and Cuie Wen*[1]

[1]*Faculty of Engineering & Industrial Sciences, Swinburne University of Technology, Hawthorn, VIC. 3122, Australia*

[2]*National Institute for Materials Science, Sengen 1-2-1, Tsukuba 305-0047, Japan*

Abstract

Corrosion behavior and microstructure of as-cast metastable β -type Ti-20Nb-xRu (x =0, 0.5, 1.0, 1.5, at.%) have been investigated using linear polarization and transmission electron microscopy (TEM), respectively.

Ruthenium (Ru) was confirmed to be a β-phase stabilizer as a titanium (Ti) alloying element which served to suppress both ω precipitation and elemental segregation; the prominence and degree of elemental segregation between the Nb-rich primary dendrites and the interdendritic areas rapidly decreased with minor Ru addition, yielding a more homogenous microstructure overall. Additionally, even minimal Ru additions significantly altered the corrosion potential (E_{corr}), yielding a 0.3V shift in the noble direction over the Ru-free controls, along with a comparable shift in the potential at which the initial passive region begins to fail (E_{inc}).The present result suggests Ru addition can confer a greater resistance to corrosion in β-Ti alloys.

Keywords
β-titanium alloys, biomaterials, corrosion, microstructure, TEM

*Corresponding author. Tel: +61 3 92145651; fax: +61 3 92145050.
Email address: cwen@swin.edu.au (C. Wen).

1. Introduction

Titanium (Ti) and some of its alloys currently represent the gold standard in biomedical implants. The reasons for this are myriad: aside from its excellent strength and low density, Ti is non-allergenic, non-carcinogenic, rapidly forms an impermeable oxide layer that greatly contributes to its corrosion resistance and, in its austenitic β-phase, can yield elastic moduli nearly as low as that of human bone [1-7]. Coupled with the potential for useful thermoelastic behavior, such as the shape memory effect (SME) and psuedoelasticity, it is clear that Ti-based alloys are promising targets for further research and development as metallic biomaterials.

Of the current generation of Ti alloys, the nickel-titanium alloy Nitinol [1] has received much attention; however, although it is lauded for its excellent shape-recovery abilities, the high concentration of the carcinogenic and allergenic nickel (Ni) is a significant concern, particularly in implants that may remain *in vivo* for protracted periods of time [2,3]. A promising alternative is the group V element, niobium (Nb), which exhibits an excellent biological response in both elemental and ionic forms [4-7], while still yielding the SME on alloying with Ti [8].

Ti is noted for its excellent resistance to corrosion due to the thin passive ceramic oxide layer on its surface; in a static environment, this oxide layer is sufficient to prevent undue corrosion, particularly given the availability of methods to further anodize or passivate Ti and its alloys beyond their natural tendency [9]. However possible issues may arise in the very applications for which shape memory alloys are best suited, those that see repeated martensitic transformations or mechanical abrasion, due to continual damage of the oxide layer, which in turn inhibits the ability of the alloy to resist corrosion and thus decreases fatigue life [10,11]. Furthermore, evidence exists that the presence of calcium (Ca) and phosphate ions in physiological systems reduces the corrosion resistance of Ti alloys [12], a

disconcerting finding given the metals' applications in orthopedic roles. These issues lead in turn to concerns about the formation of particulates and the release of ions into the surrounding tissue; although Ti is not known to be allergenic or carcinogenic, it nevertheless exhibits a degree of cytotoxicity in ionic form [6], and the ion release from Ti powders has shown to be highly detrimental to both the proliferation and viability of osteoblast-like cells cultured in proximity [4].

For this reason, it is clear that to achieve a supremely biocompatible alloy, it is necessary to further improve the corrosion resistance of Ti SMAs under adverse conditions. To this end, the Ti-Nb alloy system was chosen as a starting point in this study; in addition to the aforementioned benefits of biocompatibility and a SME, the addition of Nb has been suggested to improve the corrosion resistance of Ti alloys [13,14]. A ternary element, the platinum group metal ruthenium (Ru), was then added in varying minor amounts. The elements Ru and palladium (Pd) are both known for their ability to greatly boost the corrosion resistance of Ti even in extremely small amounts [15], and both have a history of use in dental alloys. However Ru was chosen over Pd due to both its lower cytotoxicity, and that evidence exists for Pd^{2+}, in the form of a chloride salt, acting as a carcinogen [6,16]. Furthermore, as Ru addition has until now primarily been investigated only in α+β Ti alloys, and never before in the Ti-Nb alloy system, the characterization of Ru's impact on the microstructure of metastable β-phase alloys is vital to ensure that it does not adversely affect other desirable attributes of the system.

The results of preliminary investigations into the basic microstructural and corrosion characteristics of the alloys with varying Ru contents are presented in the present investigation.

2. Materials and methods

2.1 Materials

Four compositions were investigated: Ti-20Nb, Ti-20Nb-0.5Ru, Ti-20Nb-1.0Ru, and Ti-20Nb-1.5Ru (at.% hereafter). As-cast ingots were prepared using high purity elements via cold crucible levitation melting, from which samples were cut via electrical discharge machining (EDM) into discs of thickness 2 mm, diameter 10 mm, and analyzed in the as-cast condition.

2.2 Corrosion analysis

Electrochemical corrosion analysis was performed using a potentiostat (Princeton Applied Research PARstat 2273a), with a saturated potassium chloride (KCl) calomel reference electrode (SCE) and platinum counter electrode. Potentiodynamic polarization measurements were undertaken on Ti-20Nb-xRu disc samples, while cast Ti-6Al-4V (ASTM Grade 5) and commercially pure (CP) Ti (ASTM Grade 2) was used as controls. All experiments were conducted in unaerated Hanks' balanced salt solution (HBSS) at 37 ^{o}C to simulate the physiological environment. HBSS was made using phosphate and magnesium sulfate ($MgSO_4$) salts, but without phenol red or glucose. The composition of the HBSS is given in Table 1. Samples were analyzed in two conditions, henceforth designated cleaned and aged. Samples were polished to P2400 grade SiC paper and ultrasonically cleaned in ethanol; cleaned samples were analyzed at this stage. Open circuit potential and current as a function of time following immersion in HBSS was then measured for all samples; this indicated both voltage and current appeared to stabilize by 48 hours immersion for all samples. As such, aged samples were further held at 37 ^{o}C in the HBSS for ~48 h prior to analysis. These were then mounted into the electrochemical cell with only a circular region, of approximate diameter 8 mm, exposed to solution. Measurements were conducted over the range of -0.8 to 3.5 V, with a step size of 1.00 mV and a sampling rate of 1.00 Hz. The corrosion current density (i_{corr}) was calculated from the samples aged in solution; due to the absence of a

traditional anodic Tafel slope, values of i_{corr} were instead calculated via extrapolation of the cathodic branch to the measured values for the corrosion potential (E_{corr}). Corrosion rate (CR) was determined from i_{corr} via the equivalent weight method outlined in ASTM: G102.

2.3 Microstructural analysis

Initial specimens for X-ray diffraction (XRD) analysis were prepared as with unaged corrosion samples. Specimens for microscopic observation were polished to a mirror finish with microcolloidal silica suspension (Struers OP-S). Etching for optical microscopy (OM) was performed using Kroll's reagent under ambient conditions; 2-4 minutes exposure to stirred, concentrated (5% HF, 10% HNO_3) Kroll's reagent was necessary to observe the microstructure in Ru-containing samples.

Phase characterization was performed using XRD with Cu Kα radiation (Bruker D8 Advance). Repeat analysis to elucidate α″ behavior was performed on samples polished to a mirror finish, etched in concentrated Kroll's reagent until an approximately 50 μm reduction in sample thickness was observed, and then ultrasonicated in ethanol to remove corrosion products.

Scanning electron microscopy (SEM) combined with energy dispersive spectroscopy (EDS) was performed under both secondary electron and back-scattered electron illumination (Field Emission Zeiss Supra 40 VP).

Transmission electron microscopy (TEM) samples were cut using electrical discharge machining and then mechanically ground to a thickness of approximately 80 μm. From this, TEM foils were punched and then electropolished in a solution of 6 % perchloric acid, 35 % *n*-butyl alcohol and 59 % methanol (Fischione Model 120 Twinjet). TEM observations were performed at a 200kV accelerating voltage (JEOL JEM 2000FX).

Microhardness was measured using a Vickers microindenter with a 300 g load and 10 s dwell time on the samples prepared for OM, prior to etching (Akashi MVK-E).

3. Results

3.1 Electrochemical corrosion analysis

Potentiodynamic polarization curves for fresh and aged alloy samples are presented in Figs. 1 (a) and (b), respectively, while the relevant electrochemical properties are given in Table 2. The influence of Ru addition on the corrosion behavior of Ti-Nb alloys can be clearly seen in E_{corr} for both the freshly-cleaned (E_{corrC}) and aged (E_{corrA}) samples; the Ru containing alloys all show a pronounced shift in E_{corr} in the noble (+ve) direction compared with the Ru-free alloy. In the as-cleaned samples, this is marked by an approximately 0.23 V difference to the Ru-free alloy, or 0.16 V difference relative to the CP Ti and Ti-6Al-4V controls. This appears to be independent of the magnitude of the Ru addition in the presently investigated composition range, with no statistically significant differences between E_{corrC} in the 0.5, 1.0 and 1.5% Ru containing alloys. An even greater degree of ennoblement was exhibited by the aged TiNbRu alloys, both relative to the controls and the SCE potential.

Interestingly the addition of Ru, or indeed any element, appeared to have little effect on the observed i_{corr} values for the alloys. All alloys investigated displayed an i_{corr} value of approximately 0.04 $\mu A/cm^2$, with no difference within observed uncertainty; these values agree well with those seen in other highly passive Ti alloys reported in literature [17,18].

In addition to increasing the observed E_{corr} values, allowing the alloys to come to stabilize in solution also introduced a region displaying a comparatively slower increase in current density versus potential between the values of E_{corrA} and 0.19 V (for Ti-6Al-4V) to 0.55 V (for Ti-20Nb-1.5Ru), beyond which the current density increases sharply; the potential values at which this increase occur for each alloy are given in Table 2 as E_{inc}. Between E_{corrA} and E_{inc}, all samples investigated maintained a current density below 0.4 $\mu A/cm^2$; this matches the behavior seen in similar systems [17,18], and is attributed by de Assis *et al*. to the presence of an initial highly impermeable passive film that then gradually transitions to a less protective

passive film at voltages above E_{inc}.

Subsequently, the observed current density plateaus again; this was observed at potentials above approximately 0.3V in the unaged samples, or above 0.6-0.8 V in the aged. In unaged samples, current density in this plateau region was on the order of 3-15 μA/cm^2, with no noticeable trend related to composition. However, following aging some slight variation due to composition was observed, with CP Ti and Ti-6Al-4V controls falling at approximately 3-5 μA/cm^2, a higher current density of approximately 4-10 μA/cm^2 for the Ru-containing alloys, and on the order of 5-12 μA/cm^2 for the Ti-20Nb alloy.

From this point onwards, transient spikes in current density could be observed; although many of these varied in location, number and magnitude between runs, spikes at potentials of ~1.05 and ~1.7 V SCE were detected in all alloys. These spikes are reminiscent of similar behavior observed in a Ti-Al-Nb alloy, and are considered suggestive of passive film breakdown in a manner similar to pitting nucleation of the film [18]. At ~1.2 V SCE, the current density again increases sharply, before stabilizing once more at 1.6 V SCE; this increase was most pronounced in the Ru containing alloys, although still detectable in the control samples, and is believed to arise due to the formation of new compounds such as $NaTiPO_4$ [18].

3.2 Microstructural analysis

The XRD spectra of the four as-cast Ti-20Nb-xRu (x=0.0, 0.5, 1.0 and 1.5) alloys are presented in Fig. 2. All four alloys can be seen to exhibit a microstructure consistent with a predominantly body centered cubic (bcc) β phase. However, in addition to the β-phase, faint peaks indicative of the orthorhombic α″ phase were detected in the low Ru-content alloys. To determine if this was a surface effect, or representative of the bulk material, heavy etching to remove the surface layer of material (≥50μm) was performed on all alloys; no meaningful difference was noted in the alloys with a Ru concentration ≥1.0%. In the lower Ru

concentration alloys, α″ peaks could no longer be observed, however diffraction peaks consistent with the ω-phase were now detectable.

Optical microscopy (OM) of the as-cast Ti-Nb-Ru alloys required the utilization of a highly concentrated Kroll's reagent; images are presented in Figs. 3(a)-(d), with Fig. 3(a) showing overetched (left) and lightly etched (right) surfaces of the Ti-20Nb sample at the same magnification. Alloys showed no visible evidence of precipitate phase, although dendrites were clearly visible in the Ti-20Nb case. Examples of primary grain boundaries are visible as either the broad white lines in the right image of Fig. 3(a), or as the more clearly defined dark boundaries in Fig. 3(c)-(d); in all alloys, the primary grain size shows little difference, showing an equiaxed morphology with mean diameters of approximately 1000 μm. However, etching of the Ru-containing alloys revealed a fine secondary grain structure in these alloys, which displayed a consistent mean diameter on the order of 200 μm, independent of degree of Ru addition. These secondary boundaries were not detectable in the Ti-20Nb alloy after mild etching, and increasing the degree of etching merely causes the dendritic microstructure to dominate.

SEM observation was performed on the alloy samples prior to successful etching, and observations support those of OM: equiaxed grains were observed in all four alloys, with no evidence of the acicular or platelike morphology indicative of the hexagonal α phase, while dendrites were most pronounced in the Ru-free alloy.

Analysis via energy dispersive spectroscopy (EDS) identified a periodic elemental segregation in all four alloys, corresponding to the observed dendrites. The dendrites displayed a significant enrichment of Nb relative to the surrounding material; in the nominally Ti-20Nb alloy, Nb content ranged from between 14 and 21 %, with a mean difference between dendritic and interdendritic regions of 3.7 ± 0.9 %. The mean composition differences between dendrites compared to the inter-dendritic area for the four

alloys are presented in Table 3; from this it is immediately apparent that the Ru shows little to no preference for either the Nb-rich or Nb-poor regions, and furthermore acts to mitigate the segregation of the Nb from the Ti with increasing alloy content.

Detailed microstructure characterization has been carried out on the as-cast samples using TEM. Figs. 4(a)-(d) are the typical bright field TEM micrographs. All the as-cast alloys show a predominantly β-phase structure, with heavy twinning visible as line contrast within these figures; through selected area electron diffraction (SAED), this was identified as {112}<111>-type twinning. SAED also indicated the presence of the ω-phase in all alloys; this was too fine to be resolved under bright-field illumination as in Figs. 4(a)-(d), but dark-field images obtained from the ω diffraction maxima revealed the presence of ultra-fine athermal ω-particles, with a spherical to ovoid morphology, and consistent size of 3-4 nm across all alloys. A representative dark-field image, taken from the Ti-20Nb alloy, is given in Fig. 5(a) with corresponding SAED pattern inset. These findings are consistent with work on a similar Ti-Nb-Pd alloy system by Cui et al, who observed that the ω-phase aggregated along the <111> direction within the matrix $\{112\}_\beta$ planes [19].

In addition to ω, a second precipitate phase was identified, which was ascribable to the hexagonal α′-phase; forming acicular precipitates, this α′ was observed solely in limited regions of the as-cast Ti-20Nb alloy, a representative micrograph of which is shown in Fig. 5(b).

3.3 Vickers hardness

Optical micrographs of representative indentations are presented in Figs. 6(a)-(d) for the four as-cast Ti-20Nb-xRu (x=0.0, 0.5, 1.0 and 1.5) alloys. The Vickers hardness decreased significantly with even a small addition of Ru, with the Ti-20Nb sample at 322 ± 5 Hv, followed by 280 ± 4 Hv for Ti-20Nb-0.5Ru, 272 ± 5 Hv for Ti-20Nb-1.0Ru and finally 241 ± 5 Hv for the Ti-20Nb-1.5Ru alloy. This compares favorably to the 145-200 Hv observed for

cast CP Ti in literature in a similar as-cast state, which even after significant heat treatment, rises at most to 260 Hv, though this is of course still less than the values observed for common α+β duplex alloys such as Ti-6Al-4V, at 341-369 Hv [20,21]. It also closely matches that seen for similar Ti-35Nb (wt.%) alloy recently reported by Griza *et al*., where hardness is attributed to α″ formation [22].

In addition to hardness, it is apparent that the alloy's propensity towards brittle fracture also changed with Ru concentration; noticeable cracking on the periphery of the indentations was noted in the Ru-free alloy, decreased substantially on the addition of only 0.5% Ru, and could not be observed at all for higher Ru concentration alloys.

4. Discussion

4.1 Corrosion

As is apparent from the E_{corr} and E_{inc} values reported in Table 2, Ru greatly increases the noble nature of both the Ti alloy and the passive layer formed upon ageing in a physiological solution. This occurs due to Ru's role in catalyzing the reduction of H^+, which also prevents or retards the acidification of crevice environments [23], greatly reducing the alloy's susceptibility to crevice corrosion. The addition of Ru does not noticeably alter the observed corrosion current density under open circuit conditions; however, while a reduction would be desirable, it is not vital, particularly given Ti-alloys already typically display extremely low corrosion currents, and hence corrosion rates.

One potential area for concern is the noted significant increase in current density of the Ti-20Nb-xRu alloys at higher applied voltages. Between 0.6 and 1.2 V SCE, this appears to be a function of the Nb addition, with the Ti-20Nb alloy exhibiting the highest current density in this region, but decreasing upon even minor Ru addition. However, beyond 1.2 V SCE, current density is clearly adversely influenced by the Ru addition. The mechanism by which this occurs is presently unknown; given Ru's efficacy as a catalyst, it may be that this is due

to Ru catalyzing the formation of new species, but this must be confirmed via further experimental work.

While the relative increase in current density in the highly anodic region for the Ru-containing alloys is not ideal, it is only observed at potentials beyond 1.2 V SCE; voltages that are unlikely to occur in the biological environment given the redox potentials associated with most biologically relevant species [24].

4.2 Microstructure

Although the alloy is consistently identified as predominantly β-phase, the detection of minor precipitate phases varied depending on analysis technique utilized.

The ω-phase was detected in all four alloys via TEM, and was detectable under XRD in the Ti-20Nb and Ti-20Nb-0.5Ru samples following surface etching. Although the precipitates observed under TEM were all on the order of 3-4 nm in size, and thus not expected to adversely affect brittleness or hardness of the material [19], its detection via XRD suggests that an increase in either particle size or volume fraction of ω occurs when Ru falls to 0.5 % or less; this correlates well with phase diagrams constructed by Gepreel et al [25], from which ω is expected for Ti-20Nb alloys with up to an approximately 0.6% Ru content, but should be suppressed with larger Ru contents due to the element's nature as a β-stabilizer. This would also explain in part the increase in brittle fracture observed in the same alloys, particularly when the presence of α' is considered; while the α' phase should only form below approximately 14% Nb in a binary Ti-Nb alloy [26], well below the nominal composition of the investigated alloy, it was nevertheless detected via TEM. However, given both the large compositional swings due to dendrite formation, and the sparse distribution of α'-containing regions, it is likely that the presence of α' corresponds to the most heavily Nb-depleted region. As both ω and α' are known to cause embrittlement, the increased brittle fracture in the Ru-free alloy over the 0.5 % Ru, and its absence at higher Ru contents can thus be explained.

It is also necessary to consider the metastable phase α″. This was initially detected under XRD; however, subsequent analysis via both optical and electron microscopy could find no evidence of this phase. The absence of this phase under TEM in particular is problematic, given that the volume fraction of precipitation sufficient to be detectable via XRD should be clearly evident under TEM, and samples have undergone no additional thermal processing that may induce or eliminate it. Interestingly, subsequent XRD spectra following heavy etching of the surface lacks α″ peaks, suggesting that the observed α″ may instead be a surface effect, and not representative of the bulk sample. Given α″ is a stress induced phase, the high local stresses experienced during mechanical polishing with SiC paper may be the cause; by contrast, acid etching and electropolishing both remove sample volume with minimal applied stress, and hence observation following these preparation steps would be expected to lack this phase.

4.3 Hardness

Comparing the indentation area shown in Fig. 6 to the average grain sizes (visible in Fig. 3), it is apparent that the grain size significantly exceeds the measurement area for the Ti-20Nb alloy; it is therefore unlikely that grain size is the primary contributor towards the observed hardness variation. This therefore suggests that hardness varies due to microstructural differences within the grain boundary.

As discussed in section 4.2, there was little difference in size and density of ω observed under TEM, although some change may be seen via XRD; this therefore suggests the observed hardness variation cannot be solely attributed to ω, particularly in the higher Ru-content alloys. One property that does vary across all four alloys investigated, however, is the degree of elemental segregation observed; this is significantly higher in the Ti-20Nb case, and decreases with increasing Ru, a trend that correlates well with the observed hardness.

Given that microhardness measurements occur on the scale of the dendritic features (40~50

μm), the observed hardening likely occurs due to processes comparable to Hall-Petch hardening, with the dendrite interfaces acting in a manner similar grain boundaries [27]. By increasing the Ru content, however, the magnitude of the composition variation and the barrier to deformation it represents are decreased; as such the observed variation in hardness is primarily attributed to the decreasing elemental segregation due to Ru addition, with the decreasing inhomogeneity of the dendrite interface presenting a reduced barrier to deformation.

Taken in conjunction with the precipitation of acicular α′ in the Nb-depleted regions of the Ru-free alloy, this may explain the observed behavior.

5. Conclusions

The impact of ruthenium addition on microstructure, hardness and corrosion behavior of as-cast Ti-Nb-Ru alloy have been investigated using electron and optical microscopy along with Vicker's microhardness measurements and potentiodynamic polarization.

1) Minor Ru addition (0.5 at%) significantly increased both the corrosion potential (E_{corr}) and the potential at which the initial passive film of the alloy transitions to a less protective form, reducing both the propensity for the alloy to act as an anodic site and the transient current for voltages up to +0.5V above E_{corr}, supportive of the ability of Ru addition to Ti alloys in improving resistance to corrosion.
2) Ti-20Nb-xRu (x=0.0, 0.5, 1.0 and 1.5 at%) alloys were all predominantly β-phase with a high density of fine ω precipitates and twins under TEM. While there was no observable difference under TEM, ω precipitation was detectable via XRD only in the low Ru-content alloys. This increase in ω phase is attributed to a reduced β-stabilization, supporting Ru's role as a β stabilizer.
3) Elemental segregation of Ti and Nb due to dendrite growth during casting was highly evident in the Ru-free alloy, and decreased in prominence with increasing Ru content.

This variation is sufficient to allow the formation of small quantities of α′ in the Nb-depleted regions of the Ti-20Nb alloy, and is believed to directly influence the microhardness of the observed alloys.

Acknowledgements

The authors acknowledge financial support for this research by the Australian Research Council (ARC) through the ARC Discovery Project DP110101974.

References

1 Thompson SA. An overview of nickel-titanium alloys used in dentistry. Int Endod J 2000;33:297-310.

2 Takeshita F, Takata H, Ayukawa Y, Suegetsu T. Histomorphometric analysis of the response of rat tibiae to shape memory alloy (nitinol). Biomater 1997;18:21-25.

3 McMahon RE, Ma J, Verkhoturov SV, Munoz-Pinto D, Karaman I, Rubitschek F, Maier HJ, Hahn MS. A comparative study of the cytotoxicity and corrosion resistance of nickel–titanium and titanium–niobium shape memory alloys. Acta Biomater 2012;8:2863-2870.

4 Li Y, Wong C, Xiong J, Hodgson P, Wen C. Cytotoxicity of titanium and titanium alloying elements. J Dent Res 2010;89:493-497.

5 Matsuno H, Yokoyama A, Watari F, Uo M, Kawasaki T. Biocompatibility and osteogenesis of refractory metal implants,titanium, hafnium, niobium, tantalum and rhenium. Biomater 2001;22:1253-1262.

6 Yamamoto A, Honma R, Sumita M. Cytotoxicity evaluation of 43 metal salts using murine fibroblasts and osteoblastic cells. J Biomed Mater Res1998;39(2): 331-40.

7 Biesiekierski A, Wang J, Gepreel MA, Wen C. A new look at biomedical Ti-based shape memory alloys. Acta Biomater 2012; 8(5):1661-1669.

8 Miyazaki S, Kim HY, Hosoda H. Development and characterization of Ni-free Ti-base shape memory and superelastic alloys. Mater Sci Eng A 2006;438-440:18-24.

9 Puippe JC. Surface treatments of Ti alloys. Eur Cell Mater 2003;5(1):32-33.

10 Bertacchini OW, Lagoudas DC, Patoor E. Fatigue life characterization of shape memory alloys undergoing thermomechanical cyclic loading. P Soc Photo-Opt Ins 2003;5053:612-624.

11 Akahori T, Niinomi M, Fukui H, Suzuki A. Fatigue, fretting fatigue and corrosion characteristics of biocompatible beta type titanium alloy conducted with various thermo-mechanical treatments. Mater Trans 2004;45(5):1540-1548.

12 Sousa SR, Barbosa MA. Corrosion resistance of titanium CP in saline physiological solutions with calcium phosphate and proteins. Clin Mater 1993;14:287-294.

13 Shukla AK, Balasubramaniam R, Bhargava S. Properties of passive film formed on CP titanium, Ti–6Al–4V and Ti–13.4Al–29Nb alloys in simulated human body conditions. Intermetallics 2005;13:631-637.

14 Slokar L, Matković T, Matković P. Alloy design and property evaluation of new Ti-Cr-Nb alloys. Mater Des 2012; 33;26-30.

15 Schutz RW. Ruthenium enhanced titanium alloys. Plat Met Rev 1996;40(2);54-61.

16 Schroeder HA, Mitchener M. Scandium, chromium (VI), gallium, yttrium, rhodium, palladium, indium in mice: Effects on growth and life span. J Nutrition 1971;101;1431-1438.

17 Bai Y, Hao YL, Li SJ, Hao YQ, Yang R, Prima F. Corrosion behavior of biomedical Ti-24Nb-4Zr-8Sn alloy in different simulated body solutions. Mater Sci Eng C 2013;33:2159-2167.

18 de Assis SL, Wolynec S, Costa I. Corrosion characterization of titanium alloys by electrochemical techniques. Electrochim Acta 2006;51:1815–1819.

19 Cui CY, Ping DH. Microstructural evolution and ductility improvement of a Ti-30Nb alloy with Pd addition. J Alloy Compd 2009;471:248-252.

20 Materials properties handbook: titanium alloys. Welsch G, Boyer R, Collins EW, editors. Materials Park: ASM International; 1994. p226.

21 Rocha SS, Adabo GL, Henriques GEP, Nobilo MAA. Vickers hardness of cast commercially pure titanium and Ti-6Al-4V alloy submitted to heat treatments. Braz Dent J 2006;17(2):126-129.

22 Griza S, Sá DHGdS, Batista WW, de Blas JCG, Pereira LC. Microstructure and mechanical properties of hot rolled TiNbSn alloys. Mater Des 2014; 56; 200-208.

23 King F, Watson S. A review of the corrosion performance of selected metals as canister materials for UK spent fuel and/or HLW: Appendix D Corrosion of titanium alloys. Henly-on-Thames: Quintessa; 2010.

24 Voet D, Voet JG. Biochemistry, 4th Ed. New York: John Wiley & Sons; 2010. p585.

25 Gepreel MA, Hinoshita K, Morinaga M. General approach to phase stability and elastic properties of β-type Ti-alloys using electronic parameters. Scripta Mater 2006;55:477-480.

26 Moffat DL, Kattner UR. The stable and metastable Ti-Nb phase diagrams. Metall Mater Trans A 1988;19(10):2389-2397.

27 Kaya H, Çadirli E, Böyük U, Maraşli N. Variation of microindentation hardness with solidification and microstructure parameters in the Al based alloys. Appl Surf Sci 2008;255:3071-3078.

Captions for Tables

Table 1 Chemical composition of Hank's balanced salt solution

Table 2 Electrochemical properties of titanium alloys, determined via potentiodynamic polarization in HBSS versus a SCE

Table 3 Relative elemental composition (at.%) of dendrites/Nb-enriched areas vs. inter-dendritic/Nb-depleted areas

Captions for Figures

Fig. 1 Representative potentiodynamic polarization curves of titanium alloys in HBSS: (a) freshly cleaned and (b) aged samples.

Fig. 2 XRD spectra for Ti-20Nb-xRu (x = 0, 0.5, 1.0 and 1.5) alloys. Spectra labeled with an asterisk (*) taken following extensive surface etching.

Fig. 3 OM micrographs: (a) Ti-20Nb, (b) Ti-20Nb-0.5Ru, (c) Ti-20Nb-1.0Ru and (d) Ti-20Nb-1.5Ru. Image (a) shows over-etched (left) and lightly etched (right), at same magnification.

Fig. 4 Bright-field TEM micrographs showing typical microstructure in: (a) Ti-20Nb, (b) Ti-20Nb-0.5Ru, (c) Ti-20Nb-1.0Ru and (d) Ti-20Nb-1.5Ru. Note the high density of {112}<111>-type twins.

Fig. 5 Representative TEM micrographs of precipitate phases, both taken from the as-cast Ti-20Nb alloy: (a) A typical dark field TEM image revealing the fine ω precipitates with the corresponding SAED pattern inset. (b) A typical bright field TEM micrograph showing the morphology of α′ precipitates (indicated by arrow) with the corresponding SAED pattern inset.

Fig. 6 OM images of the representative Vickers indentations: (a) Ti-20Nb, (b) Ti-20Nb-0.5Ru, (c) Ti-20Nb-1.0Ru and (d) Ti-20Nb-1.5Ru alloy samples.

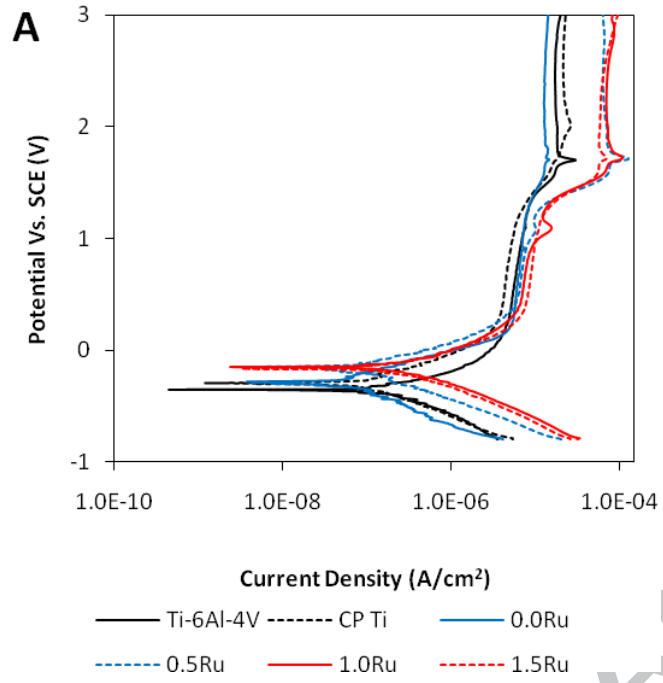
A
Potential Vs. SCE (V)
3
2
1
0
-1
1.0E-10
1.0E-08
1.0E-06
1.0E-04
Current Density (A/cm²)
Ti-6Al-4V
CP Ti
0.0Ru
0.5Ru
1.0Ru
1.5Ru

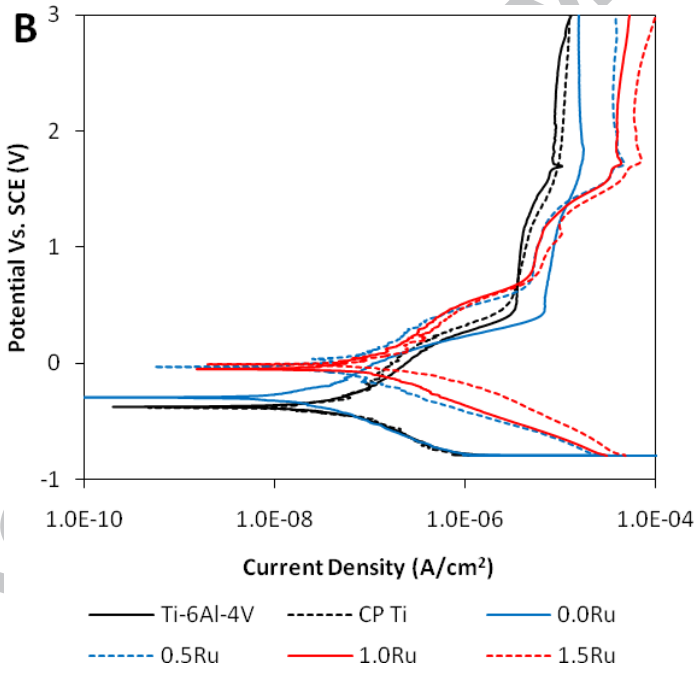
B
Potential Vs. SCE (V)
3
2
1
0
-1
1.0E-10
1.0E-08
1.0E-06
1.0E-04
Current Density (A/cm²)
Ti-6Al-4V
CP Ti
0.0Ru
0.5Ru
1.0Ru
1.5Ru

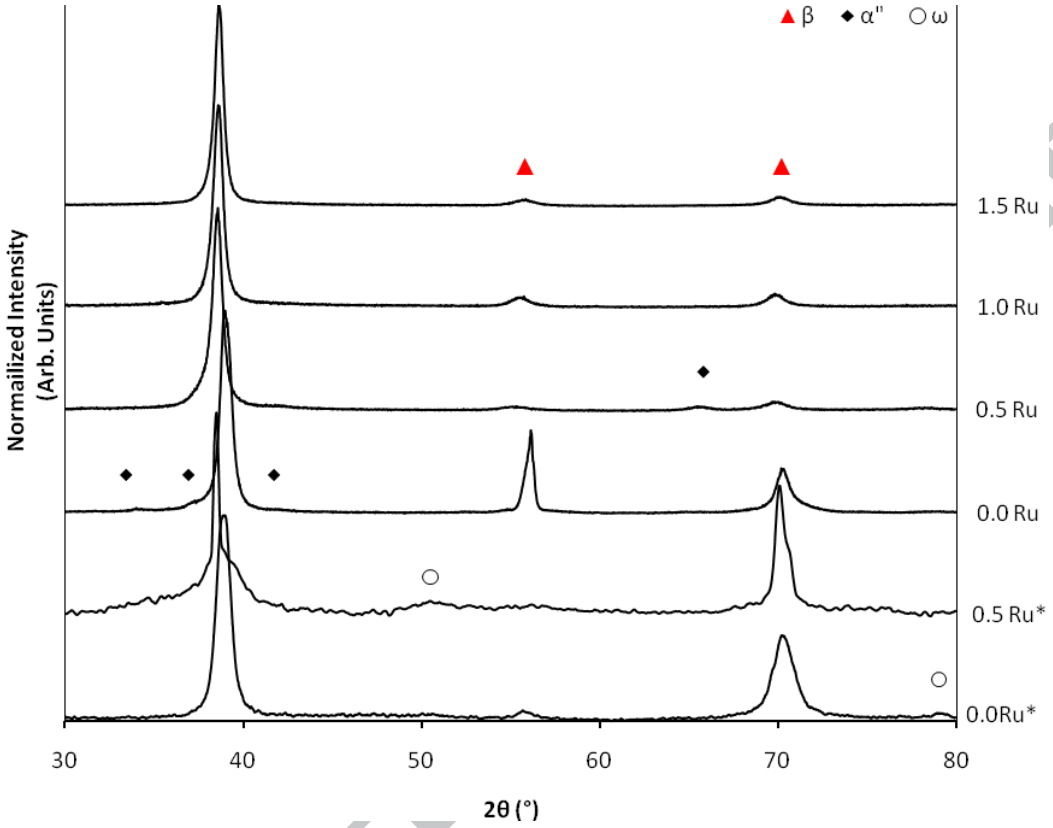

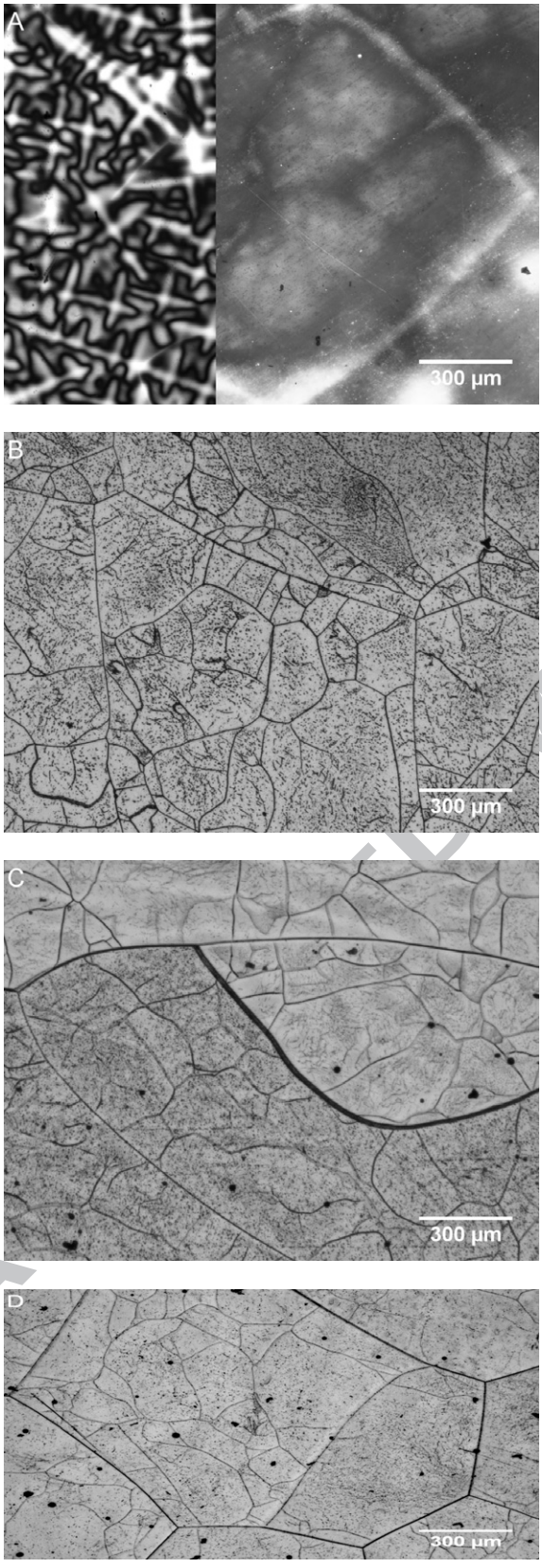

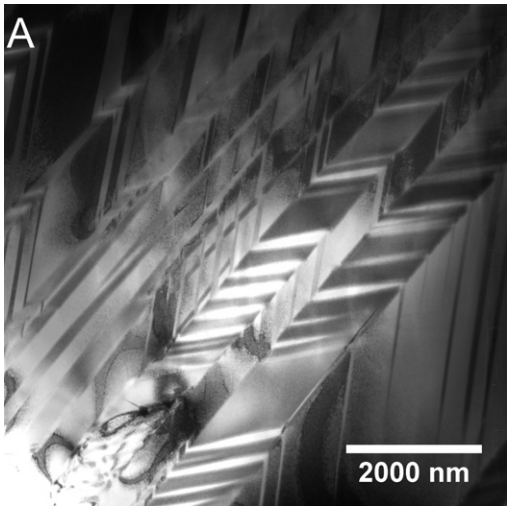

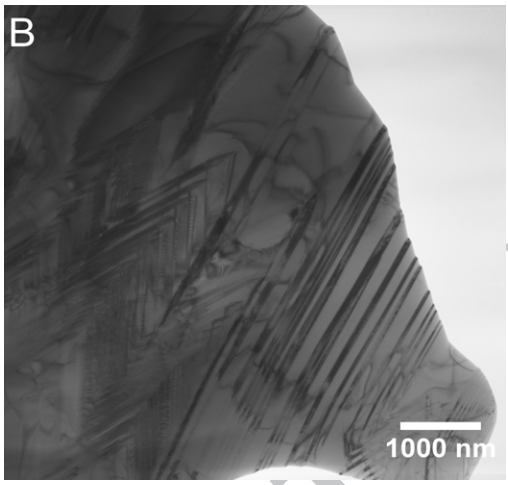

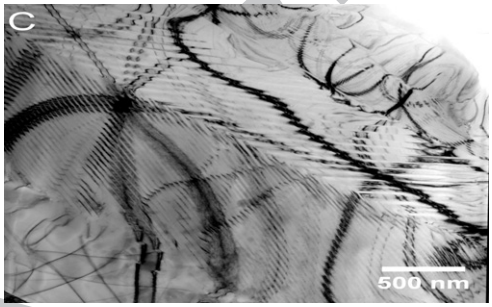

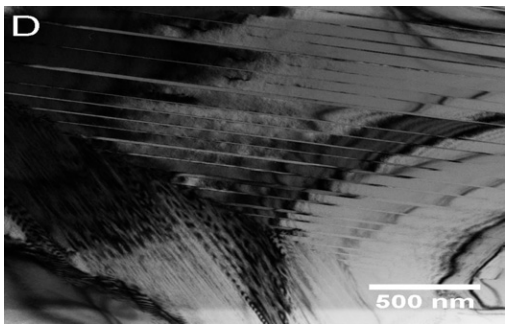

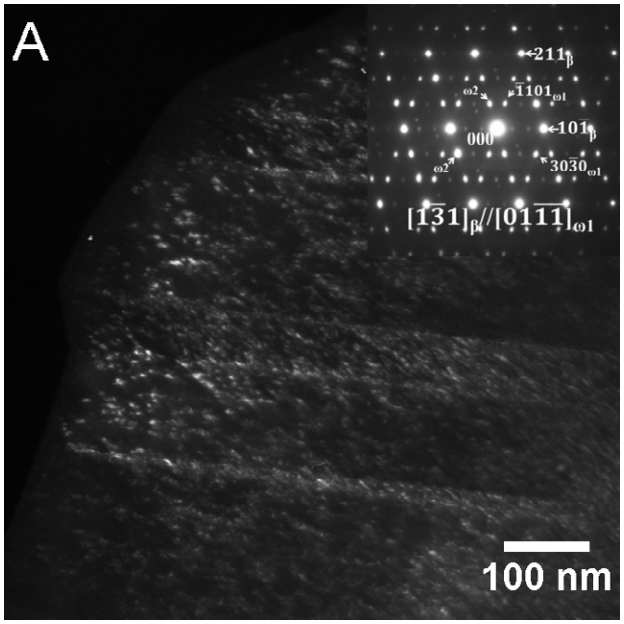

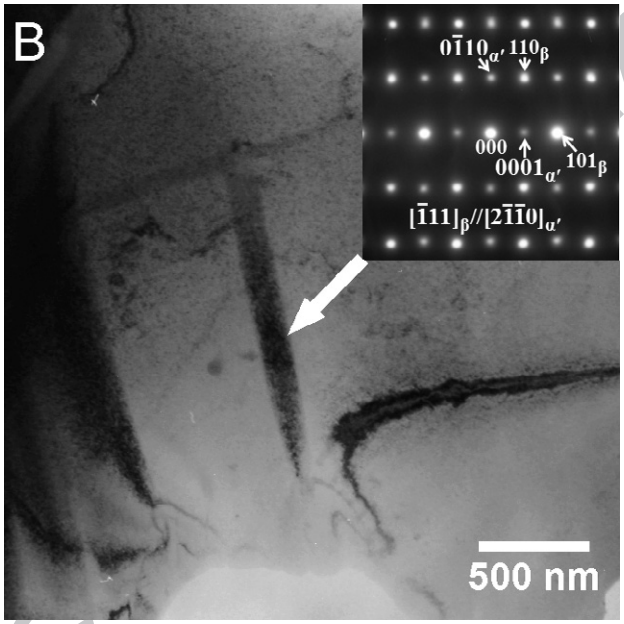

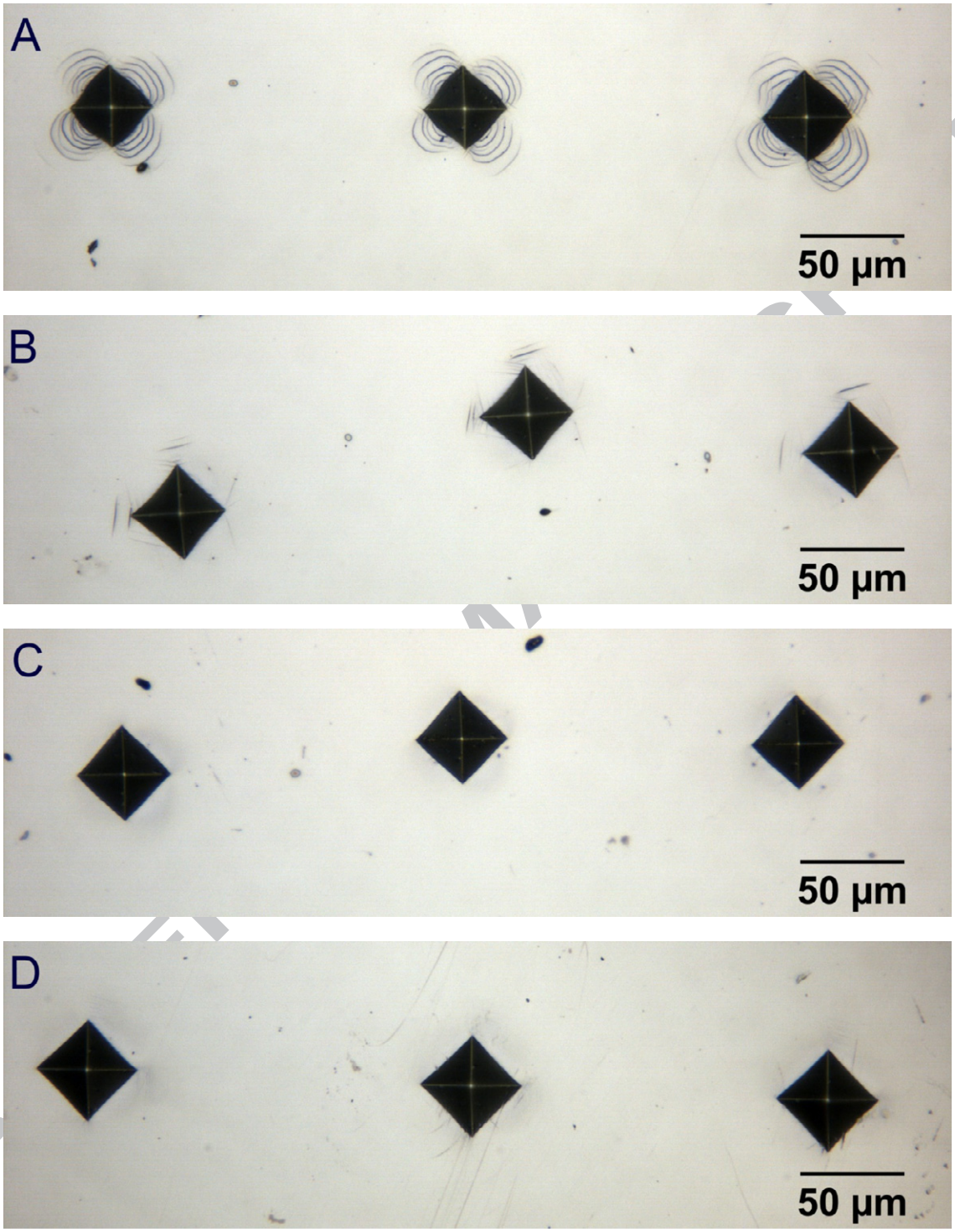
A
50 µm
B
50 µm
C
50 µm
D
50 µm

Table 1 Chemical composition of Hank's balanced salt solution

Compound	Concentration (mol/L)
NaCl	0.1370
KCl	0.0054
$CaCl_2.2H_2O$	0.0013
$Na_2HPO_4.2H_2O$	0.0003
KH_2PO_4	0.0004
$MgSO_4.7H_2O$	0.0010
$NaHCO_3$	0.0042

Table 2 Electrochemical properties of titanium alloys, determined via potentiodynamic polarization in HBSS versus a SCE

	E_{corrC} (V)	E_{corrA} (V)	E_{inc} (V)	i_{corr} (μA/cm^2)	CR (mm/yr)
Ti-6Al-4V	-0.32 ± 0.05	-0.28 ± 0.08	0.19 ± 0.05	0.04 ± 0.02	0.4 ± 0.2
CP Ti	-0.33 ± 0.03	-0.28 ± 0.09	0.30 ± 0.03	0.04 ± 0.02	0.4 ± 0.2
Ti-20Nb	-0.4 ± 0.2	-0.34 ± 0.09	0.22 ± 0.03	0.04 ± 0.02	0.3 ± 0.2
Ti-20Nb-0.5Ru	-0.15 ± 0.03	-0.05 ± 0.03	0.49 ± 0.04	0.04 ± 0.01	0.25 ± 0.07
Ti-20Nb-1.0Ru	-0.17 ± 0.03	-0.04 ± 0.05	0.49 ± 0.08	0.04 ± 0.03	0.3 ± 0.2
Ti-20Nb-1.5Ru	-0.13 ± 0.06	-0.04 ± 0.07	0.55 ± 0.03	0.036 ± 0.004	0.27 ± 0.03

Error = 1 Std. Dev.

Table 3 Relative elemental composition (at. %) of dendrites/Nb-enriched areas vs. inter-dendritic/Nb-depleted material

	Ti	Nb	Ru
Ti-20Nb	-3.7 ± 0.9	+3.7 ± 0.9	-
Ti-20Nb-0.5Ru	-1.3 ± 0.2	+1.5 ± 0.3	-0.2 ± 0.1
Ti-20Nb-1.0Ru	-0.9 ± 0.3	+0.8 ± 0.5	+0.1 ± 0.2
Ti-20Nb-1.5Ru	-0.6 ± 0.2	+0.7 ± 0.2	-0.1 ± 0.3

Error = 1 Std. Dev.

Highlights

- Ti-20Nb-xRu alloys (x = 0.0, 0.5, 1.0, 1.5 at.%) were investigated.
- Microstructure, hardness and corrosion properties are presented.
- Ru addition increases noble nature of alloys.
- Ru stabilizes the BCC β phase and reduces precipitation of the ω phase.
- Elemental segregation of Ti and Nb also decreases with increasing Ru addition.